

## **Abstract**

IN PROGRESS

# Contents

<b>Aims and skills</b>	<b>1</b>
<b>1 Heavy Stable Charged Particles (HSCPs)</b>	<b>2</b>
1.1 Motivations for New Physics searches . . . . .	2
1.2 Overview of HSCPs in supersymmetric models . . . . .	2
1.2.1 Tau sleptons ( $\tilde{\tau}$ ) . . . . .	3
1.2.2 Identification methods: Time-of-Flight (TOF) delay . . . . .	3
1.3 Recent developments . . . . .	3
<b>2 The Large Hadron Collider (LHC)</b>	<b>4</b>
<b>3 The Compact Muon Solenoid (CMS) Experiment</b>	<b>5</b>
3.1 Detector coordinate system and parameters . . . . .	5
3.2 Detector design (subdetectors) . . . . .	5
3.2.1 The trackers . . . . .	6
3.2.2 The electromagnetic calorimeter (ECAL) . . . . .	6
3.2.3 The hadronic calorimeter (HCAL) . . . . .	6
3.2.4 The superconducting solenoid . . . . .	6
3.2.5 The muon system . . . . .	6
<b>4 Time-Of-Flight (TOF) analysis</b>	<b>7</b>
<b>5 Candidate matching and kinematic variable analysis</b>	<b>9</b>
5.1 Generated-to-generated candidate matching . . . . .	9
5.2 Generated-to-reconstructed candidate matching . . . . .	11
5.3 Generated vs reconstructed $1/\beta$ values . . . . .	11
<b>6 Efficiency analysis</b>	<b>12</b>
6.1 Reconstruction efficiency . . . . .	12
6.2 Level-1 muon trigger efficiency . . . . .	12
<b>7 Real data (muon) kinematic analysis</b>	<b>19</b>
<b>Conclusions and outlook</b>	<b>20</b>
<b>Bibliography</b>	<b>20</b>

# Aims and skills

The programming languages used for the analyses presented in this thesis were Python and C++, with an emphasis on the latter. The CMS SoftWare (CMSSW) framework was used to extract and analyse information from simulated, reconstructed and real data. This required how to navigate the documentation of the framework. The analyses were then summarised on plots produced using the CERN ROOT framework.

# Chapter 1

## Heavy Stable Charged Particles (HSCPs)

### 1.1 Motivations for New Physics searches

While the Standard Model has proven time and again that it is a fairly robust summary of the building blocks of matter, it still has its shortcomings. For example, the model's failure for the

### 1.2 Overview of HSCPs in supersymmetric models

In supersymmetry each SM fermion (boson, spin 1) has a SUSY boson (fermion, spin 1/2) partner.

No particular SUSY model was investigated in this thesis, as the analysis concerned the general phenomenology of SUSY particles.

Heavy Stable Charged Particles (HSCPs) are (at the time of writing at least) theoretical long-lived particles (LLPs). LLPs are also present in

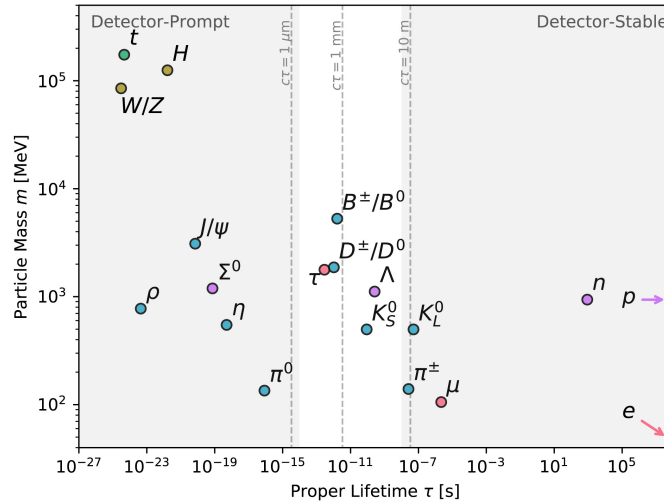


Figure 1.1: A summary of the lifetimes of the SM particles. Neutrinos are examples of LLPs within the SM. 'Detector-Stable' means that the decay of a particle within the detector material is highly unlikely.

### 1.2.1 Tau sleptons ( $\tilde{\tau}$ )

The focus of this study were tau sleptons ( $\tilde{\tau}$ ), which are the supersymmetric partners of SM tau leptons ( $\tau$ ). In Monte Carlo simulations, ( $\tilde{\tau}$ ) candidates are assigned the number 1000015 if they are the SUSY partner of a left-handed  $\tau$ , and 2000015 if they are the SUSY partner of a right-handed  $\tau$  [1]. In particular, the  $\tilde{\tau}$  candidates analysed in this thesis were pair produced. This implies that  $R$ -parity was conserved.

### 1.2.2 Identification methods: Time-of-Flight (TOF) delay

There are two primary tools that can be used to identify HSCPs tranversing through detectors. The first is the expectation of a significantly larger energy loss in trackers for HSCPSs, compared to SM particles, due to HSCPs having a much higher mass. This will not be discussed further. The second method is the Time-of-Flight (TOF) identification method.

## 1.3 Recent developments

The interest in searches for HSCPs at the LHC experiments has recently peaked, due to an unexpected result coming from the ATLAS<sup>1</sup> experiment. The mass distribution presented in figure 1.2

**FIGURE**

*Figure 1.2: Mass distribution*

However, the aforementioned TOF analysis method eliminated the possibility that the observed excess was due to particles of a HSCP nature.

---

<sup>1</sup>ATLAS - A Torroidal LHC ApparatuS, the largest LHC experiment.

## Chapter 2

# The Large Hadron Collider (LHC)

The Large Hadron Collider (LHC) is the largest cyclic particle accelerator of the CERN accelerator complex on the Franco-Swiss border, with the headquarters of CERN located on the outskirts of Geneva. It is the largest

**FIGURE**

*Figure 2.1*

## Chapter 3

# The Compact Muon Solenoid (CMS) Experiment

The Compact Muon Solenoid (CMS) experiment[2] is one of the four experiments permanently installed on the LHC ring, located at Point 5 (P5).

### 3.1 Detector coordinate system and parameters

## FIGURE

*Figure 3.1: The global coordinate system of the CMS detector. The  $x$  axis points towards the centre of the LHC ring, the  $y$  axis is orientated directly upwards, and the  $z$  axis follows the LHC beampipe (anticlockwise). Shown also are the azimuthal ( $\phi$ ) and polar ( $\theta$ ) angles -  $\phi$  is measured anticlockwise from the  $x$  axis in the  $xy$  plane, and  $\theta$  is measured anticlockwise from the  $z$  axis in the  $yz$  plane.*

### 3.2 Detector design (subdetectors)

The detector is considered to be hermetic/ $4\pi$ , which means that the interaction point (IP) of the two beams is surrounded by many different subdetectors in order to reconstruct collision

events as fully as possible. Moving outwards from the IP, the subdetectors are: the trackers (pixel and strip), the electromagnetic calorimeter (ECAL), the hadronic calorimeter (HCAL), the superconducting solenoid and the muon system. The subdetectors are discussed in greater detail below, based on their structures during Run-2 (2015-2018) of the LHC.

### **3.2.1 The trackers**

The tracking system of the CMS experiment can be split in two, namely: the pixel tracker and the strip tracker. In both cases the tracking elements are made of silicon. During Run-2 [and Run-3? check whether something changed here...] the pixel tracker was composed of [number] elements of dimensions [dimensions]. The pixel tracker is the closest subdetector to the IP.

### **3.2.2 The electromagnetic calorimeter (ECAL)**

### **3.2.3 The hadronic calorimeter (HCAL)**

### **3.2.4 The superconducting solenoid**

The solenoid operates with a magnetic field strength of 3.8 T. It is the largest solenoid magnet ever produced.

### **3.2.5 The muon system**

The muon system is the outermost subdetector of the CMS detector, and the only subdetector outside of the magnet. Therefore, the direction of the magnetic field This subdetector is known for its redundancy, containing an abundance of elements available for particle detection. This improves the overall efficiency of the muon system. The muon system can be split into three regions, in which different reconstruction algorithms called muon track finders (MTFs), are used. These regions are: the barrel (BMTF,  $|\eta| < 0.83$ ), the overlap (OMTF,  $0.83 < |\eta| < 1.24$ ) and the endcaps (EMTF,  $|\eta| > 1.24$ ). The latter has the upper boundary of  $|\eta| < 2.4$ . During Run-2, the muon system was composed of three types of muon chambers, namely: cathode strip chambers (CSCs), drift tube (DT) chambers, and resistive plate chambers (RPCs). These are outlined below.



## Chapter 4

# Time-Of-Flight (TOF) analysis

The simulated analysis presented in this chapter was performed on a data sample of 100 events containing pair-produced  $\tilde{\tau}$  of mass 200.86 GeV. This sample contains all of the final state (status 1) particles from the Pythia generation of full events. In order to eliminate the analysis of SM leptons also present in the sample, a condition was set to only consider candidates with particle IDs exceeding 1E6.

While in practice there is no guarantee that pair production of  $\tilde{\tau}$  occurs at the exact interaction point of the two proton beams (known also as the *beam spot*), the convention in the CMSSW framework is to take the origin of the collision coordinate system (0,0,0) when considering generated data [**empty citation**]. This is not to be confused with the centre of the CMS detector, as the IP can shift along the  $z$  axis between collisions (although in truth this can be even a few cm from the geometric centre of the detector, which, considering the size of the detector, is a practically negligible distance).

An initial look at the hit information showed that the SL2 coordinate system was indeed different from the systems of SL1 and 3, as per figure ???. A summary of hits from one DT chamber in event 1 is shown in table ??. It can be seen that hits 5-8 have a different [sign?] in *can'tremember*.

|

Table 4.1: Caption

# FIGURE

*Figure 4.1*

The question that followed this was whether the hits would be correctly translated to the global detector frame (see figure 3.1).

## Chapter 5

# Candidate matching and kinematic variable analysis

It must be stressed that the next two chapters are about results obtained using a different, as well as significantly larger, data sample than the simulated data analysis. The reason for this is that no data sample contained both simulated and reconstructed data was made available to the author. Therefore, the analyses presented in the next two chapters are based on 85000 events containing pair-produced  $\tilde{\tau}$  of mass 431.822 GeV.

The first task was to perform basic candidate matching between the generated and reconstructed HSCP candidates. This was done on the basis of the  $\Delta R$  parameter. This parameter is calculated using:

$$\Delta R = \sqrt{(\Delta\eta)^2 + (\Delta\phi)^2} = \sqrt{\quad} \quad (5.1)$$

where  $\eta_1/\phi_1$  and  $\eta_2/\phi_2$  are the two candidates under consideration for matching.

### 5.1 Generated-to-generated candidate matching

In general the matching process of generated-to-generated candidate matching was performed as a sanity check to make sure that the generated  $\tilde{\tau}$  pairs behaved as expected when produced (i.e. they did not travel in vaguely the same direction, see figure ??).

## FIGURE

*Figure 5.1: Schematic diagram showing an example of incorrect back-to-back production (in red - this would give a very small  $\Delta R$  value) and correct back-to-back pair production (in green).*

??

The duplicate pairs have been removed by imposing a condition that if generated particle  $A$  has already been matched to generated particle  $A'$ , then the matching process should not occur again for  $A'$ . This was relatively simple to implement, given that each event had only one generated  $\tilde{\tau}$  pair. Figure 5.2 presents the result of the matching process for all events.

## FIGURE

*Figure 5.2: Plot for  $\Delta R$  for all generated-to-generated pairs in each event in the data sample, with duplicates removed. As expected, all of these pairs are 'back-to-back', meaning that the particles traversed in opposite directions from the production point.*

It can be seen that there is a peak at around  $\pi$  - this is confirmation that the candidates were produced back-to-back, although it is not clear whether this is back-to-back with respect to  $\eta$  or  $\phi$ . Therefore, for completeness, the distributions of  $\Delta\eta$  and  $\Delta\phi$  were also investigated, and are shown in figure 5.3.

**FIGURE**

**FIGURE**

*Figure 5.3: The distributions for  $\Delta\eta$  (left) and  $\Delta\phi$  (right). From these two figures, it can be seen that the back-to-back matches seen in figure 5.2 tend to be back-to-back in [insert parameter here]/equally back-to-back in  $\phi$  and  $\eta$ /other.*

## 5.2 Generated-to-reconstructed candidate matching

In the case of generated-to-reconstructed candidate matching, there is no possibility of duplicate matches. Instead, the task is to identify the matches with the smallest  $\Delta R$  values, and only consider these in further analyses.

**FIGURE**

*Figure 5.4: Plot for  $\Delta R$  for all generated-to-reconstructed pairs in each event in the data sample. The peak on the left includes all of the generated-to-reconstructed pairs that can be considered to have been matched correctly (i.e.  $\Delta R$  is very small). The second peak shows 'back-to-back' pairs of generated and reconstructed candidates (i.e. the generated particle traversed in the opposite direction to the reconstructed particle).*

## 5.3 Generated vs reconstructed $1/\beta$ values

(5.2)

## Chapter 6

# Efficiency analysis

Efficiency calculations relating to the reconstruction and recording of SUSY candidates are important in understanding how well existing software and hardware tools may respond to such particles. In this section, the results of efficiency calculations with respect to two tools are presented: the Monte Carlo based reconstruction, and the L1 muon trigger response. The efficiency, defined here as ( $\epsilon$ ), in this study was defined by:

$$\epsilon = \frac{X_{gen,probe+trig}}{X_{gen,probe}} \quad (6.1)$$

in which  $X_{gen,probe}$  refers to the total number of generated candidates passing initial cuts applied to the generated candidates only. The  $X_{gen,probe+trig}$  term is the number of generated candidates passing initial and secondary cuts, with the latter applied to both themselves and their reconstructed counterparts. The efficiency plots were created using the ROOT TEfficiency class, which calculated  $\epsilon$  on the basis of weights. In this particular case, generated . The efficiency was calculated with respect to four different kinematic parameters, namely:  $p_T$ ,  $p$ ,  $\eta$  and  $1/\beta$ . The first three parameters were extracted straight from the physics objects, while  $1/\beta$  was calculated using formula 5.2.

The errors on the presented efficiency plots are calculated using the Clopper-Pearson (CP) confidence level calculation method. [summarise CP method for CL calculations]

### 6.1 Reconstruction efficiency

The  $\Delta R < 0.1$  condition used previously has been applied for all of the efficiency plots presented.

### 6.2 Level-1 muon trigger efficiency

For the L1T efficiency plots, the  $\Delta R$  condition was increased to  $< 0.4$ , which was decided based on the profile of figure 6.1. Similarly to before, this figure accounts for all possible combinations of generated candidates and L1 objects in each events. The L1 trigger object kinematic parameter values may not necessarily closely resemble those of the generated particles, which can be observed on the left plot of figure ?? as the tail of the left peak - this was not present on either of the plots in figure 5.4. With a tighter constraint, such as the previously used 0.1, some matched pairs would be incorrectly disregarded. The 0.4 cutoff is more clearly visible on the right plot of figure ?. The results of this matching are shown in figure 6.1.

# FIGURE

Figure 6.1: The result of the matching of generated  $\tilde{\tau}$  candidates to L1 muon trigger objects. All possible pairs per event were taken into consideration. Left: linear y-axis, right: logarithmic y-axis.

The efficiency of the L1T with respect to  $p_T^{GEN}$ ,  $p^{GEN}$ ,  $\eta^{GEN}$  and  $1/\beta^{GEN}$  for  $\tilde{\tau}$  candidates are shown in figures 6.2-6.5.

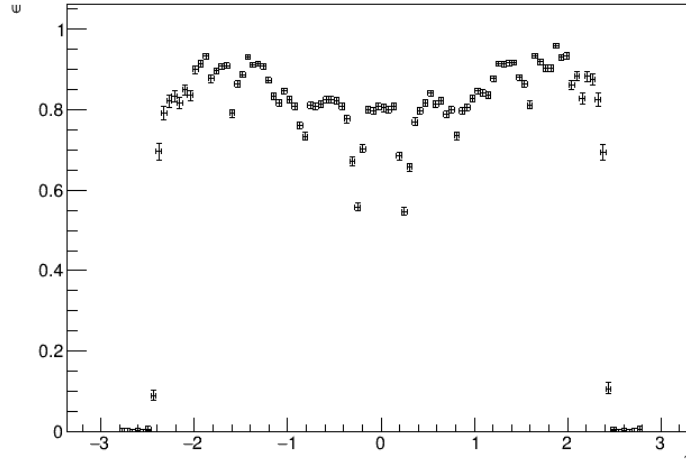


Figure 6.2: The L1 muon trigger efficiency with respect to  $p_T^{GEN}$ .

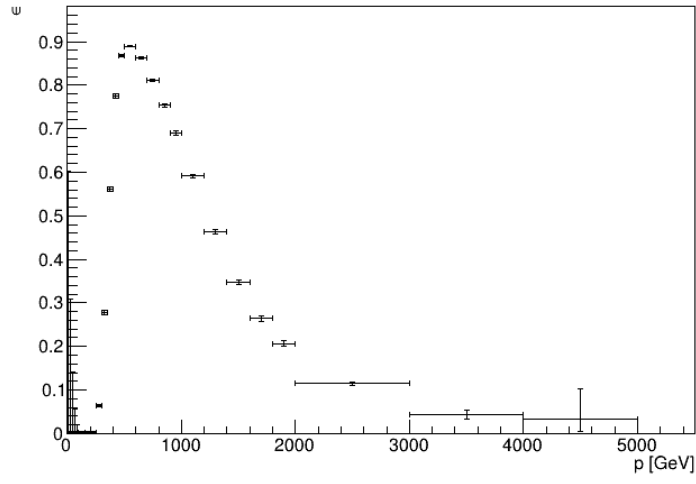


Figure 6.3: The L1 muon trigger efficiency with respect to  $p^{GEN}$ .

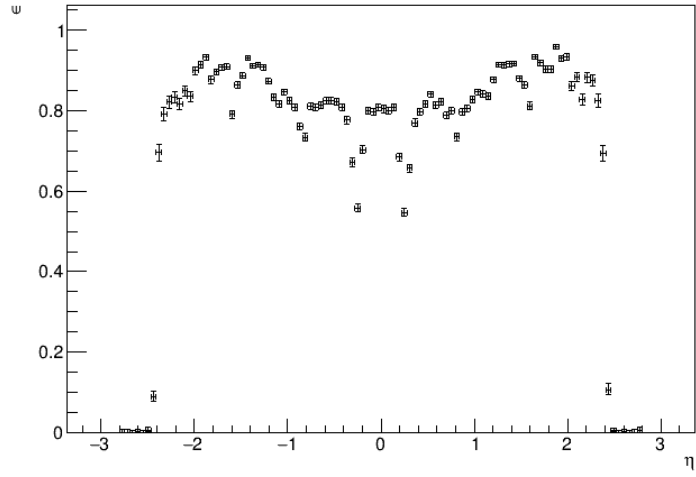


Figure 6.4: The L1 muon trigger efficiency with respect to  $\eta^{GEN}$ .

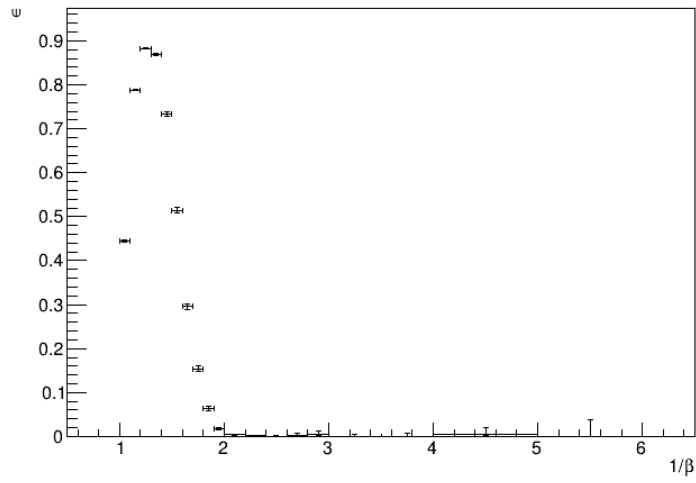




Figure 6.5: The L1 muon trigger efficiency with respect to  $1/\beta^{GEN}$ .

Figure 6.5 exhibits strange behaviour in the bin. It is expected that the efficiency will remain high at this point, but here it falls to an efficiency of [check percentage + CLs]. This led to a thorough investigation into the kinematic properties of the generated candidates passing all of the imposed conditions. For this, figures 6.6 and 6.7-6.9 were produced. These plots are efficiency maps for  $(\eta^{GEN})$  and  $(\phi^{GEN}, 1/\beta^{GEN})$ . The latter has been produced for the three regions of the muon system, with different binwidths used for each one.

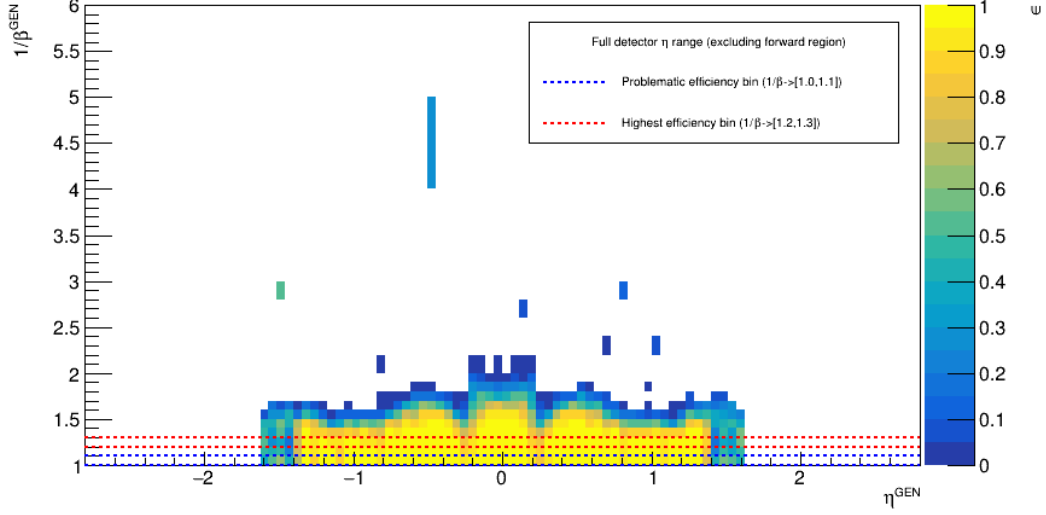


Figure 6.6: Efficiency map for  $(\eta^{GEN}, 1/\beta^{GEN})$ . Two bins from figure 6.5 are plotted. It can be seen that beyond  $|\eta^{GEN}| > 1.4$  the efficiency dramatically falls,.

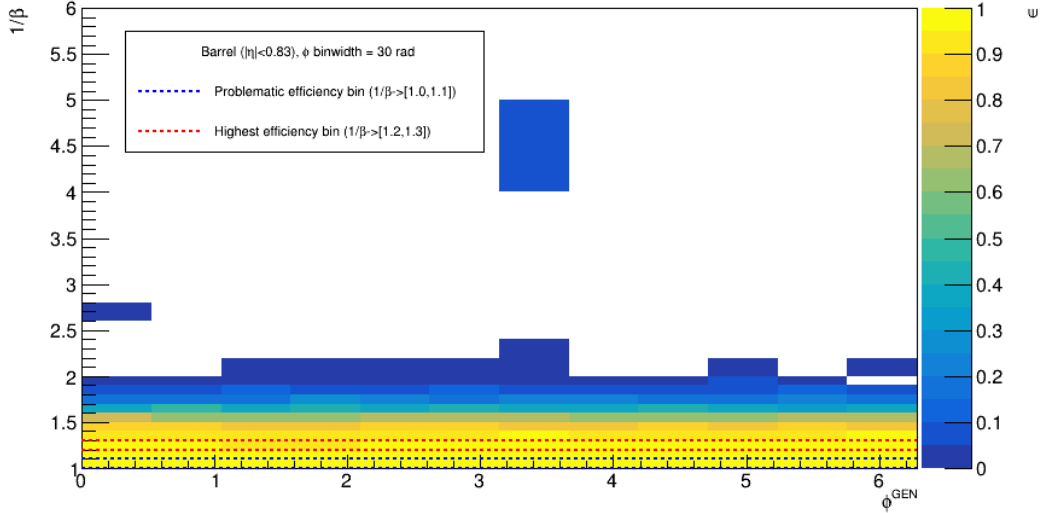


Figure 6.7: Efficiency map for  $(\phi^{GEN}, 1/\beta^{GEN})$  in the barrel region ( $|\eta^{GEN}| < 0.83$ ).

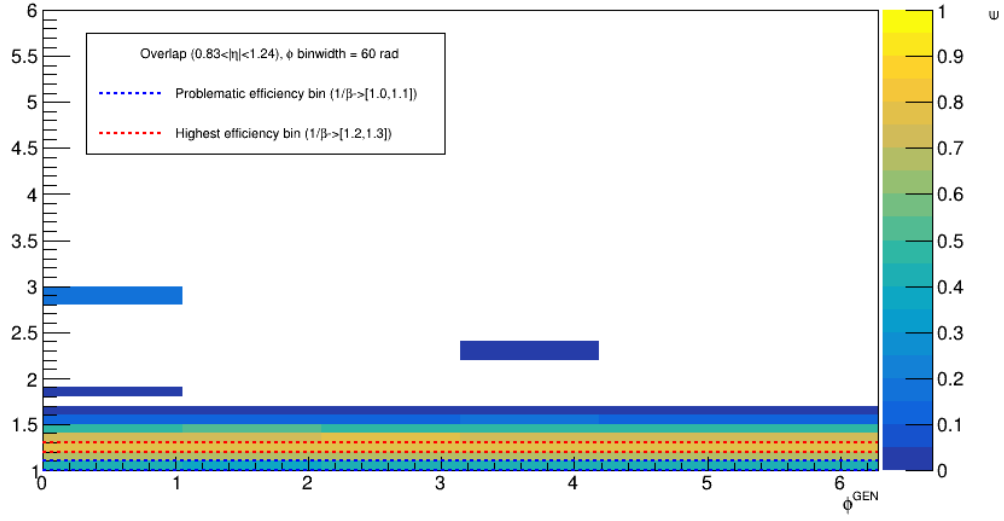


Figure 6.8: Efficiency map for  $(\phi^{GEN}, 1/\beta^{GEN})$  in the overlap region ( $0.83 < |\eta^{GEN}| < 1.24$ ).

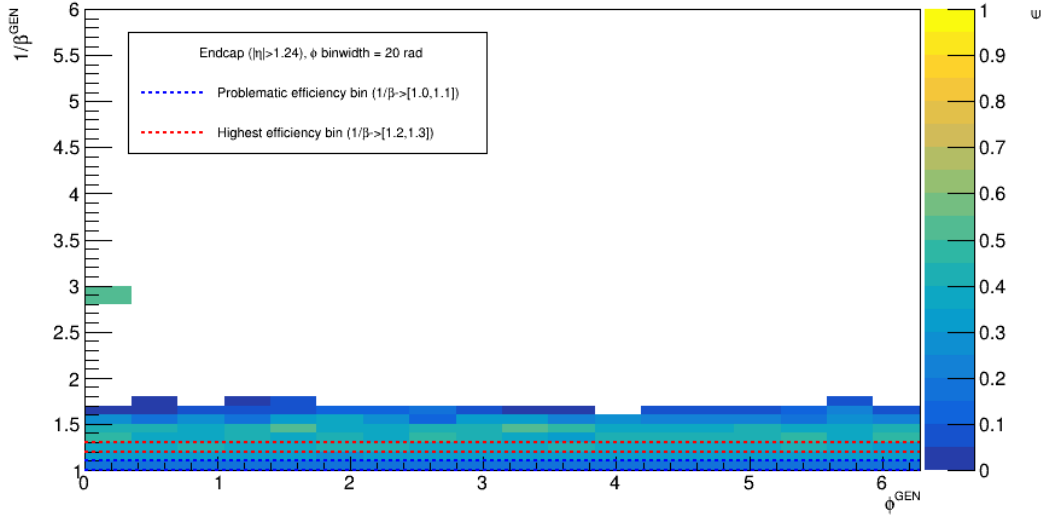


Figure 6.9: Efficiency map for  $(\phi^{GEN}, 1/\beta^{GEN})$  in the endcap region ( $|\eta^{GEN}| > 1.24$ ).

The condition for  $|\eta|$  for the efficiency plots with respect to  $p_T^{GEN}$ ,  $p^{GEN}$  and  $1/\beta^{GEN}$  was changed to 0.83 based on the above four plots, removing the OMTF and EMTF regions from the efficiency analysis.

## FIGURE

*Figure 6.10: Improved L1 muon trigger efficiency with respect to  $p_T^{GEN}$ .*

## FIGURE

*Figure 6.11: The L1 muon trigger efficiency with respect to  $p_T^{GEN}$ .*

## FIGURE

*Figure 6.12: The L1 muon trigger efficiency with respect to  $\eta^{GEN}$ .*

## FIGURE

*Figure 6.13: The L1 muon trigger efficiency with respect to  $1/\beta^{GEN}$ .*

It was found that the most plausible reason for these results was that the data had indeed been incorrectly reconstructed, with an incompatible CMSSW version. As both the OMTF and EMTF regions contain CSCs, this has been put down to an issue with their settings in the software. Also, if one looks at the full  $(\eta^{GEN}, 1/\beta^{GEN})$

## Chapter 7

# Real data (muon) kinematic analysis

The analysis presented below was conducted using real detector data collected in 2022<sup>1</sup>. It takes into consideration the L1T muons from 805 events. The  $1/\beta$  distribution of these muons is presented in figure 7.1.

## FIGURE

*Figure 7.1:  $1/\beta$  distribution for L1T muons from real data sample taken from Run-2.*

---

<sup>1</sup>The CMSSW version used for this analysis is slightly newer than for the previous chapters, but this does not affect the comparison between them.

# Conclusions and outlook

At the time of writing, no experimental evidence confirming the existence of SUSY has been found at the LHC or other colliders.

# Bibliography

- [1] Particle Data Group (**PDG**). *Review of Particle Physics*. PTEP 2022 (2022) 083C01. 2022.
- [2] **CMS** Collaboration. *CMS Physics: Technical Design Report Volume 1: Detector Performance and Software*. CERN-LHCC-2006-001;CMS-TDR-8-1. CERN, Geneva, 2006.